Highly compact TiO$_2$ films by spray pyrolysis and application in perovskite solar cells

Alexander Möllmann[a], Dawit Gedamu[b], Paola Vivo[c], Robert Frohnhoven[a], Daniel Stadler[a], Thomas Fischer[a], Ibrahima Ka[b], Maximilian Steinhorst[e], Riad Nechache[b], Federico Rosei[d], Sylvain G. Cloutier[b], Thomas Kirchartz[e], and Sanjay Mathur[a]*

[a] *Department of Chemistry, Inorganic Chemistry, University of Cologne, 50939 Cologne, Germany*

[b] *École de technologie supérieure (ÉTS) Department of Electrical Engineering, 1100 rue Notre-Dame Ouest Montréal (QC), H3C 1K3, Canada*

[c] *Department of Chemistry and Bioengineering, Tampere University of Technology, Finland*

[d] *Centre Énergie, Matériaux et Télécommunications, INRS, 1650 Boulevard Lionel Boulet, Varennes, QC J3X 1S2, Canada*

[e] *IEK5-Photovoltaics, Forschungszentrum Jülich, 52425 Jülich, Germany*

* Corresponding author email: sanjay.mathur@uni-koeln.de

ABSTRACT

Transparent and pinhole free hole-blocking layers such as TiO$_2$ grown at low temperatures and by scalable processes are necessary to reduce production costs and thus enabling commercialization of perovskite solar cells. Here we compare the transport properties of TiO$_2$ compact layers grown by spray pyrolysis from commonly used titanium diisopropoxide bisacetylacetonate ($[Ti(OPr^i)_2(acac)_2]$) precursor to films grown by spray pyrolysis of TiCl$_4$.

Spray pyrolysis provides insights into the interdependence of precursor chemistry and electron transport properties of TiO_2 films and their influence on the performance of the perovskite solar cells. X-ray diffraction and X-ray photoelectron spectroscopy data confirmed the chemical and structural composition of the obtained films. Thin film deposition at lower temperature (150 °C) were conducted using $TiCl_4$ to evaluate the influence of crystal growth and topography by scanning electron microscopy and atomic force microscopy as well as thickness (profilometry) and transmittance (UV/Vis spectroscopy) on the power conversion efficiency of perovskite solar cells. TiO_2 compact layers grown from $TiCl_4$ enhanced the power conversion efficiency by acting as superior electron transfer medium and by reducing hysteresis behavior, when compared to films grown using titanium diisopropoxide bisacetylacetonate. UV/Vis spectroscopy and external quantum efficiency studies revealed the correlation of transmittance on the power conversion efficiency.

KEYWORDS: perovskite solar cells, photovoltaics, TiO_2, spray pyrolysis, low temperature

INTRODUCTION

Over the past decade, hybrid perovskite solar cells (PSC) based on methyl ammonium lead halides ($CH_3NH_3PbX_3$; X = Cl, Br, I) as photoabsorber layers have been studied extensively, driven by the rapid increase in power conversion efficiency (PCE), which now exceeds 22%[1, 2]. In addition, the straight forward and low temperature processing of PSCs, compared to silicon photovoltaics make them promising candidates for commercialization[3, 4]. Both organic and inorganic components can be substituted in the ABX_3 composition to obtain perovskites with different A-site (e.g., methyl-ammonium (MA)[5, 6], formamidinium (FA)[7, 8] or cesium[9, 10]) and B-site (e.g., lead[11, 12], bismuth[13, 14] or tin[15, 16]) cations while commonly used anions

(X) are iodide[17, 18], bromide[19] or chloride[20] ions. For lead perovskite materials, the A and X site have been systematically interchanged to achieve high efficiency, reproducibility and environmental stability, which are the three main challenges in the processing of perovskite solar cells.[21, 22]

The large amount of data available on perovskite absorber materials suggests that an increase in the performance of the electron transfer material (ETM) may lead to higher PCE and improved stability and can also reduce the hysteretic behavior in PSCs which describes the mismatch of the J-V curves depending on the voltage sweep direction decreasing the averaged power output.[23, 24] Several materials have been tested as ETMs, including TiO_2[25, 26], SnO_2[27, 28], ZnO[29, 30] and WO_3[31]. The ETM often consists of a bilayer constituted by a compact (c-TiO_2) and mesoporous titania (m-TiO_2) junctions engineered to reduce hysteresis and improve charge transfer.[32, 33] For this purpose, TiO_2 films have been deposited using various techniques, like spin-coating[34-36], spray pyrolysis[37, 38] and atomic layer deposition (ALD)[39] to control their grain size, conformity and compactness.

Spray pyrolysis of a suitable chemical precursor is a process commonly used in industry to deposit ceramic films because of its simple and scalable nature.[40] However, the use of spray pyrolysis for PSCs has been limited so far, due to the need for high substrate temperatures (450 °C), which are essential to obtain dense TiO_2 layers. Reducing the deposition temperature and finding a precursor which results in a dense and efficient ETM layer at and below 450 °C to lower energy requirements and the possibility to deposit TiO_2 on flexible substrates is still a major challenge. However there is a wide agreement that precursor chemistry plays an important role on the morphology and crystallinity of the resulting films and metastable precursors can allow to grow compact titania films at lower temperatures.[41, 42] $TiCl_4$ has been reported to produce pinhole free films and smooth layer that reduce hysteresis.[43-45] In addition, it was tested in combination with different solvents such as water, isopropanol, tetrahydrofuran and copolymers by using chemical bath or spin-coating. One example is a precipitation

3

approach resulted in crystalline rutile TiO_2 layers at low temperatures.[46] A different approach, first deposited titanium containing precursors on the substrate and after annealing at 450 °C, an TiO_2 anatase phase layers was obtained with low surface roughness of 11 to 36 nm.[44, 47, 48]

The presence of chloride ions on the surface of compact TiO_2 layers and at the interface between the TiO_2/perovskite grain boundaries were shown to suppress deep trap states and reduce interface recombination. This was supported by density functional theory (DFT) calculations, showing that chloride ions can act as passivation layer at the TiO_2/perovskite boundary by reducing Pb-Cl anti-site defects, which in turn suppress trap states. The passivation of the interface increased the open-circuit voltage (V_{oc}) from 1.04 V to 1.14 V and the fill factor (FF) from 69 % to 77 % and additionally delivered higher stability lasting over 500 hours with retention of 90 % of the initial efficiency.[49, 50]

We report herein a comparative study on the fabrication and functional behavior of TiO_2 dense layers deposited by spray pyrolysis from $TiCl_4$ and the state of the art $Ti(OPr^i)_2(acac)_2$ precursors and discuss the influence of precursor chemistry on the PCE of hybrid perovskite solar cells.

The TiO_2 blocking layers were deposited using TDBA or $TiCl_4$ as precursors in spray pyrolysis in the temperature range 150–450 °C. For the sake of simplicity, TiO_2 blocking layers obtained from different processes are denoted as **A-450**, **A-360**, **A-270** and **A-150** for samples deposited at 450, 360, 270 and 150 °C. Similarly, the films obtained from TDBA at 450 °C were denoted **B-450**, whereas the mixed layers were **AB-450** (3x TDBA and 2x $TiCl_4$ at 450 °C).

EXPERIMENTAL SECTION

Chemicals. Fluorine-doped tin oxide (FTO) substrates (TEC 7, 2 mm), titanium diisopropoxide bis(acetylacetonate) (TDBA) (75 wt. % in isopropanol), titanium(IV) chloride (puriss., ≥99.0 % AT), cesium iodide (99.999%), spiro-MeOTAD (99%, HPLC grade) and bis(trifluoromethane)sulfonimide lithium salt (Li-TFSI, 99.95%) were purchased from Sigma-

Aldrich. Furthermore 18NR-T TiO_2 nanoparticle paste and tris(2-(1H-pyrazol-1-yl)-4-tert-butylpyridine)cobalt(III)tri[bis-(trifluoromethane) sulfonimide] (FK209 Co(III), >98%) were purchased from Dyesol. PbI_2 (99.999%) and $PbBr_2$ (99.999%) were obtained from TCI Europe. Formamidinium iodide (FAI) and methylammonium bromide (MABr) were synthesized following recipes reported elsewhere.[51, 52] Dimethyl sulfoxide (DMSO, extra dry, 99.7+%), N,N-dimethylformamide (DMF, extra dry, 99.8%), chlorobenzene (extra dry, 99.8%), acetonitrile (99.9%) from Acros Organics and absolute ethanol (Fisher Scientific, HPLC grade) were used as solvents. 4-*tert*-butylpyridine (4-TBP) was bought from Fluorochem.

Preparation of spray solution. For the preparation of spray solutions, $TiCl_4$ (0.54 ml) was added drop wise into ice cooled absolute ethyl alcohol (25 ml) to obtain 0.2 M solution. A reference spray solution was prepared by adding TDBA (2.43 g) into a flask and filling it up to 25 ml with absolute ethyl alcohol to obtain 0.2 M concentration.

Preparation of c-TiO₂ layers. FTO glass substrates, 2×2 sq. cm, were mechanically partially grinded with a TimberTech manual driller. The FTO substrates were then sonicated in an aqueous solution of Hellmanex III (0.5 - 2% wt.), DI water and absolute ethanol for 20, 15 and 10 min at room temperature, respectively. Before spraying, the substrates were treated with UV-ozone for 15 min to remove organic residuals and increase surface wetting properties. The perovskite solar cell fabrication steps are visualized in Figure 1 and are explained in detail in the following paragraphs.
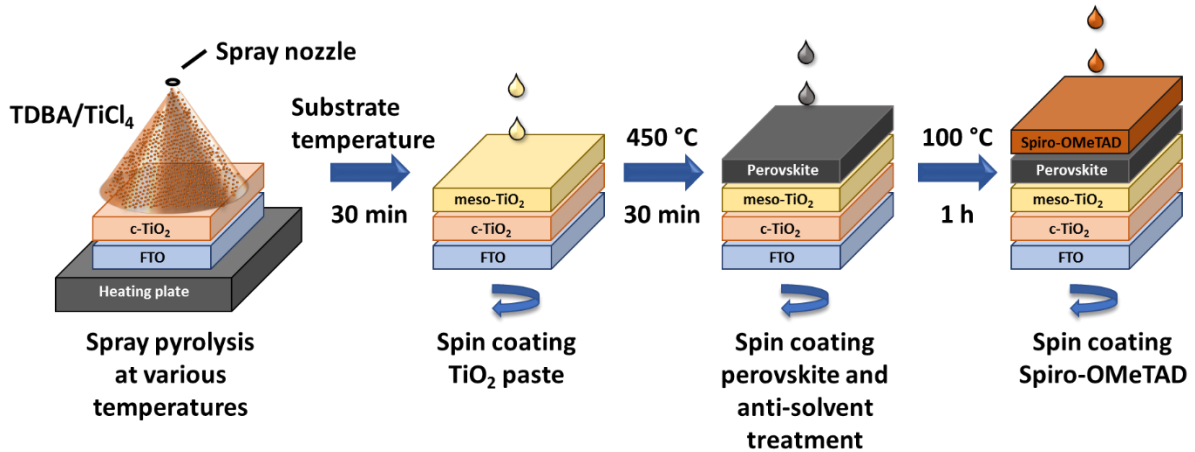
Figure 1: Schematic diagram of the perovskite solar cell fabrication process.

Subsequently, a TiO_2 compact layer was sprayed and pyrolyzed at 450 °C using an Aldrich® chromatography sprayer (10 ml). The spray pyrolysis was conducted by spraying five cycles of TDBA or $TiCl_4$ precursor solution. Furthermore, a mixed compact TiO_2 layer was prepared by spraying three cycles TDBA solution and two cycles $TiCl_4$ solution to analyse the effect of different precursors. A typical cycle consisted of 2 s spraying followed by a 10 s pause to evaporate any residual solvent. The distance between sprayer and substrate was 7 cm. After spraying, the substrates were left for 30 min at the same temperature. For the depositions at lower temperature, the spray parameters were kept constant except the substrate temperature was changed to 360, 270, and 150 °C, respectively. The relative humidity was within in the range of 35 – 45%. For grazing incident X-ray diffraction (XRD), TiO_2 layers were deposited on glass substrates instead of FTO. For scanning electron microscopy (SEM) and atomic force microscopy (AFM), sprayed titanium oxide layers were heated to 450 °C for 30 min to simulate the annealing step used for burning organic binders of the TiO_2 nanoparticle paste for the preparation of a mesoporous TiO_2 layer.

Device Fabrication. For this purpose, the substrates were cooled down to 150 °C and directly transported to a dry nitrogen filled glovebox. The mesoporous TiO_2 scaffold layer was prepared by spin coating an ethanolic suspension (4:1 wt%) of 18NR-T TiO_2 nanoparticle suspension paste at 4500 rpm, 2000 rpm/s for 30 s. The films were dried at 100 °C for 10 min prior to calcination at 500 °C for 20 min using a heating rate of 200 °C/h at air.

The perovskite solution was prepared in a N_2-filled glovebox and contained FAI (0.9 M), PbI_2 (1.1 M), MABr (0.18 M), $PbBr_2$ (0.2 M) in anhydrous DMF:DMSO 4:1 (v:v). CsI was predissolved in DMSO (1.5 M) and 80 µl of this solution was added to the perovskite solution to achieve a 10 mol% Cs concentration. The solution was spin coated onto the mesoporous TiO_2 layers at 1000 rpm with 500 rpm/s acceleration for 10 s, directly followed by 6000 rpm with 2500 rpm/s acceleration for 20 s. Afterwards, 100 µl chlorobenzene were spin coated to facilitate film growth. The perovskite recipe and spin coating procedure are reported elsewhere.[21] The perovskite layers were annealed at 100 °C for 1 h.

After annealing, a spiro-OMeTAD layer was spin coated at 4000 rpm, 2000 rpm/s acceleration for 45 s. The solution was prepared by adding 72.3 mg spiro-OMeTAD to 1 ml chlorobenzene and 28.3 µl 4-TBP. 17.5 µl Li-TFSI solution and 29 µl FK209 predissolved in acetonitrile were added to the spiro-OMeTAD solution with concentrations of 520 mg/ml and 300 mg/ml, respectively. After deposition, the cells were transferred to a desiccator filled with dry air (relative humidity <10%) and were left there overnight. Finally, a 70 nm thick gold contact was thermally evaporated on top of the spiro-OMeTAD layer to form the back contact. Evaporation was conducted in a vacuum of 5×10^{-4} mbar with an evaporation rate of 0.2 nm/s. The completed solar cells were transferred back to a desiccator for one-night prior to measuring.

CHARACTERIZATION

Characterization of c-TiO₂ layers. The imaging and analysis of surface morphology were performed with an atomic force microscope (Park Systems XE-100) operating in true non-contact mode. A cantilever of the type PPP-NHCR-10 from Nanosensors was used. The measurements were done in air and the scan size was 5×5 µm^2 with a scan speed of 1 Hz as well as a tip radius of curvature <10 nm to obtain images with 256×256 pixel resolution. XEI 1.8.0 software was used to determine the roughness average (R_a), RMS (root mean-square) surface roughness (R_q) and the maximum height of the profile (R_{pv}) which is the vertical distance between the deepest valley and highest peak.[53] SEM images were taken using a FE-SEM from Hitachi of the type SU-8230 and a Nova Nano SEM 430 from FEI. Thicknesses were determined using a profilometer of Ambios XP200 (Ambios technology Inc.). Transmittance spectra were recorded with a spectrometer of the type Lambda 950 from Perkin-Elmer. Crystallinity and phase of TiO₂ compact layer were analyzed using Bruker's D8 Advance X-ray diffractometer (XRD). For the grazing incident X-ray diffraction (GI-XRD) a 2θ range of 20 - 60° with a step size of 0.02° was chosen. The crystallite size was determined using the Scherrer equation. An approximate equation written in excel was used to calculate the crystallite sizes based on the GI-XRD pattern. XPS analysis was performed with an *ESCA M-Probe* instrument from Surface Science Instruments. The sample was irradiated with Al-K$_\alpha$ rays ($\lambda = 8.33$ Å). Survey scans were recorded using a detector pass energy of 158.9 eV. The relative humidity was measured with a Bluelans Hygrometer.

Characterization of Devices. The current (J) - voltage (V) characteristics of the solar cells were measured using a 2420 Series SourceMeter (Keithley instruments) and a WACOM-WXS-140S-Super-L2 class AAA sun simulator with a two lamp Xenon/Halogen lamp system to simulate the AM 1.5G sunlight. The spot size area was 140×140 mm^2 and the power density of illumination was 100 mWcm^{-2}, calibrated with a mono crystalline silicon reference cell. The

devices were contacted using a contact box and masked with a laser patterned 200 µm thick metal plate (aperture 0.15 cm^2). No preconditioning was applied such as light soaking or bias voltage. The light soaking was prevented by using a black cardboard which masked the other cells on the same substrate, while one was measured. In order for the V_{oc} to be ~90% of the maximum applied potential, the sweep range between 0.2 V to 1.2 V was chosen.[54] The sweep rate used was 10 mV/sec. Furthermore, the forward (-0.2 V to 1.2 V) and concurrently the reverse (1.2 V to -0.2 V) *J-V* scan was conducted. For each stack, 6–22 cells were characterized by *J-V* scans and the open-circuit potential (V_{oc}), fill factor (*FF*), short-circuit current (J_{sc}) and power conversion efficiency (PCE) were extracted from each *J-V* scan (forward and reverse).

The external quantum efficiencies (EQE) were taken with a set-up consisting of a 150 W Xenon lamp (Mueller), a grid monochromator (Benthman), an optical filter (Schott) to match the AM 1.5G spectra and a Femto 1E7V/A lock-in amplifier. The chopper frequency was set to 72 Hz and a planar-convex lens 1×3 mm was used to focus the light spot. Maximum power point (MPP) tracking was conducted by applying a constant potential of 0.78 V which was determined to be the voltage at MPP by analysing the I-V curves over time and measuring the photocurrent density under 1 sun condition.

RESULTS

Compact TiO$_2$ Layer. TABLE I summarizes the morphology, resistivity and thickness values of the prepared TiO$_2$ layers. The thickness was kept constant (ca. 30 nm) for deposition processes performed at and above 360 °C. It was found to increase slightly for **A-270** to 60 nm and drastically to above 300 nm for **A-150** which indicates different growth rates of the TiO$_2$ layer and lower degree of densification at lower temperatures. Denser films were obtained when the solvent evaporated before the droplet reaches the surface.

TABLE I: Surface roughness, thickness and resistivity of spray pyrolyzed TiO$_2$ films.

Sample	R$_a$ [nm]	R$_q$ [nm]	R$_{pv}$ [nm]	Thickness [nm]	Bulk Resistivity [Ω cm]
B-450	12	16	108	30	2,031
AB-450	12	15	114	30	469
A-450	11	14	94	30	759
A-360	12	15	99	35	5033
A-270	13	16	114	60	6026
A-150	-	-	-	300-600	-

The AFM measurements (TABLE I and Figure 2) exhibited that the TiCl$_4$ precursor resulted in smoother layers. The topography of the TiO$_2$ layers (Figure 2b-f) showed the features of the underlying FTO substrate pattern (Figure 2a), which is due to the low thicknesses (30–60 nm). **A-150** could not be measured because of its rough surface.
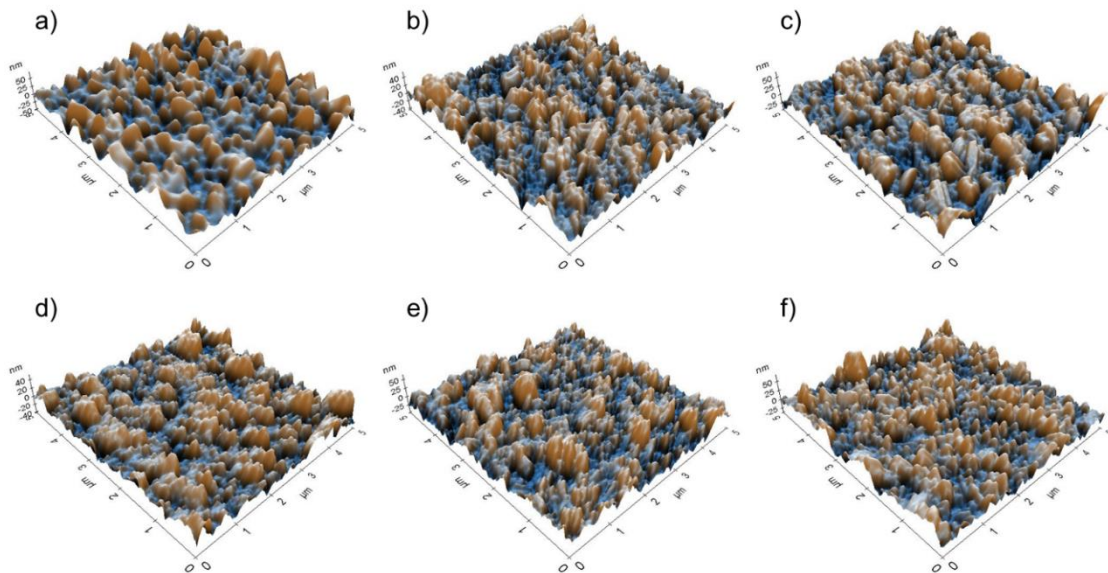

Figure 2: 3D AFM topography images of different c-TiO$_2$ layers: a) bare FTO, b) **A-270**, c) **A-360**, d) **A-450**, e) **AB-450**, f) **B-450**.

SEM images of **A-150** (Figure 3a) revealed that cracked structures with grains in the micrometer range were obtained because of the slow precursor evaporation at low spray temperatures. **A-270** (Figure 3b) and **A-360** (Figure 3c) did not exhibit any extensive pinholes. By juxtaposing the SEM images of **A-450** (Figure 3d) and **B-450** (Figure 3f), it can be observed

that the **B-450** coating consists of a layer decorated with nanometer sized particles while **A-450** exhibited a smoother surface. SEM-images of **AB-450** (Figure 3e) indicated two different layer formations on top of each other. A smooth layer which was similar to **A-450** surface and nanometer sized particles decorating the surface, as **B-450** indicated.
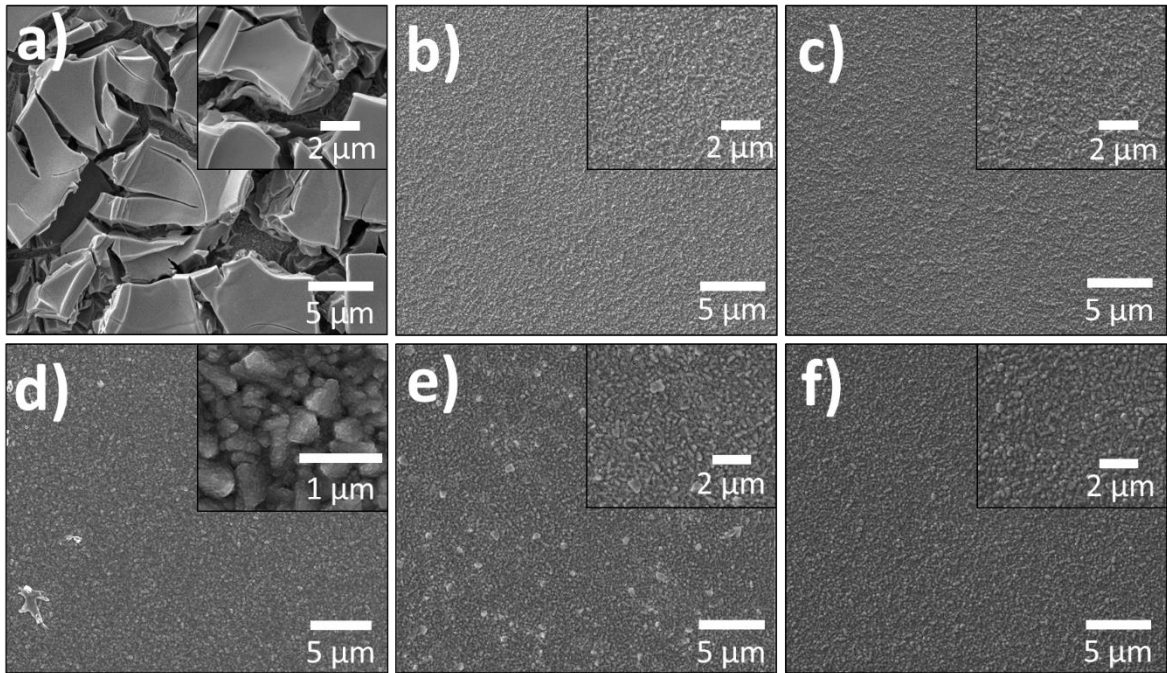

Figure 3: Surface SEM images of (a) **A-150**, (b) **A-270**, (c) **A-360**, (d) **A-450**, (e) **AB-450** and (f) **B-450**.

Transmittances measured to evaluate the suitability of prepared compact TiO_2 layers for PSCs (Figure S1) showed a slight decrease in transmittance (~5%) in the range of 400 to 800 nm when the growth temperature was reduced from 360 to 270 °C, probably due to the presence of residual organics. More than 80% of the light was not transmitted in **A-150** samples due to significant scattering losses caused by cracks and voids (Figure 3 and S1). The bulk resistivity extracted from figure S2 was found to increase from 759 Ω cm for **A-450** to 6026 Ω cm for **A-270** with decreasing deposition temperature. **A-450** was further investigated in terms of crystallite size, crystallinity and presence of surface chlorine groups which could improve the charge transfer of the TiO_2/perovskite interface. To determine crystallinity, GI-XRD (Figure

4a) measurements were conducted and peaks at 25.3°, 37.8°, 48.1°, 53.9° and 55.1° were assigned to the (101), (004), (200), (105) and (211) planes of anatase phase for **A-450**, respectively. The crystallite size was calculated from the peak broadening to be 20 nm.

The XPS survey measurement of **A-450** was conducted to evaluate the surface composition. The spectra confirmed the formation of TiO_2 but also revealed the presence of carbon (Ti: 17.6%; O: 43.9% and C: 38.5%) that can emerge from surface adsorbates as well as solvent molecules (Figure 4b). The absence of chlorine peaks at characteristic binding energies (Cl 2p: 200-202 eV, Cl 2s: 270 eV) indicates the complete decomposition and desorption of $TiCl_4$. Furthermore, an absence of a Si 2p peak and Sn 3d peak of the substrate material at approximately 100 eV and 920 eV indicated a pinhole-free layer formation.
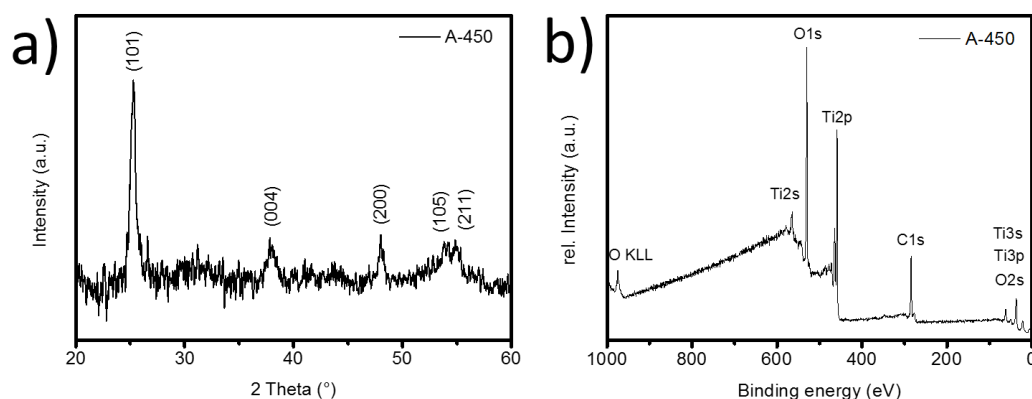

Figure 4: a) GI-XRD of the **A-450** showing peaks assigned to the anatase phase (PDF: C21-1272). b) XPS survey spectrum of **A-450** with peaks assigned to elemental orbitals based on their characteristic binding energies.

Device performance. The photovoltaic performance of prepared PSCs with different TiO_2 layers was compared using the parameters extracted from J-V curves and EQE spectra (TABLE II). The PCEs of solar cells obtained using **B-450** and **AB-450** were found to be comparable with efficiencies of 10 % and 12.5 %, respectively, and are close to the PCE values of **A-450** PSCs with 9.5 % and 11.4 %. However, an increase in the *FF* for the forward measurement

from an average of 61 % to 67 % is observed while the V_{oc} decreased from ~1 V for the **B-450**

and **A-450** sample to ~0.98 V (Figure 5a). The J_{sc} also decreased from 16.7 mA/cm^2 to 15.3

mA/cm^2. The series resistances remain identical with values of around 6.6 Ω cm^2, respectively.

Three representative J-V curves for PSCs with **B-450**, **AB-450** and **A-450** are shown in Figure

S3a) – c).

**TABLE II. Photovoltaic parameters of PSCs using B-450, AB-450, A-450, A-360, A-270
and A-150. The mean values such as *PCE*, *FF*, *V*$_{oc}$, *J*$_{sc}$, series resistance (*R*$_s$), and their
standard deviation were derived from the *J-V* curves (forward and reverse sweep).**

Sample	No.	*PCE* [%]	*FF* [%]	V_{oc} [V]	J_{sc} [mA/cm^2]	R_s [Ω m^2]
B-450	22	Forward: 10.0±1.0	61±4	1.00±0.03	16.5±2.0	
		Reverse: 12.5±1.8	74±4	1.01±0.03	16.9±2.0	6.7±2.1
AB-450	16	Forward: 10.2±0.8	65±4	0.99±0.02	16.0±1.0	
		Reverse: 12.4±0.9	75±3	1.00±0.02	16.6±1.1	6.5±1.1
A-450	14	Forward: 9.5±2.5	67±3	0.97±0.01	14.9±1.2	
		Reverse: 11.4±1.0	75±5	0.98±0.01	15.6±0.8	6.7±1.1
A-360	12	Forward: 10.8±0.6	65±2	0.99±0.02	16.9±0.5	
		Reverse: 12.0±0.8	70±4	1.00±0.01	17.0±0.6	7.5±1.1
A-270	12	Forward: 9.6±0.9	63±2	0.99±0.02	15.6±1.6	
		Reverse: 10.3±2.3	69±3	0.99±0.04	15±2.5	9.6±3.5
A-150	6	Forward: 3.0±0.3	44±2	0.65±0.02	10.8±0.7	
		Reverse: 3.4±0.2	46±2	0.65±0.01	11.2±0.4	14.9±1.8

Subject to the ETM processing conditions, the hysteresis among **B-450**, **AB-450** and **A-450**

samples was found to gradually decrease. To quantitatively evaluate the hysteresis, the absolute

and percentage change of PCEs between the forward and reverse sweep measurement was

calculated for each cell and averaged for each stack (TABLE SI). Both values decreased from

20% and 2.5% to 16% and 1.8%, respectively, corresponding to the change in the film properties originating from change in the precursor from TDBA to TiCl$_4$.
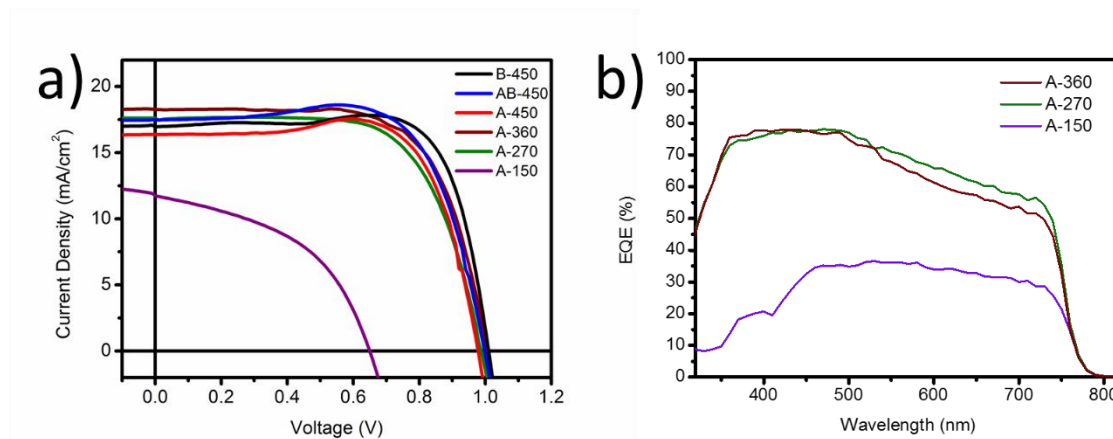

Figure 5: a) *J-V* curves of the reverse scan (from 1.2 to -0.1 V) for representative PSCs with different deposited TiO$_2$ blocking layer. b) EQE of A-150, A-270 and A-360 PSCs.

Comparing PCEs of samples obtained from **A-360**, **A-270** and **A-150** ETM layers, the PSC with **A-360** showed the highest efficiency of 10.8% for the forward sweep and 12% for the reverse sweep matching the performance of the reference PSC (**B-450**). The PCE decreased from 10.3 % in the reverse sweep for the **A-270** cells down to 3.4 % for **A-150** cells. The *FF* decreased from 65 %, to 63 % and 44 % for the forward sweep for the solar cells using c-TiO$_2$ layers deposited at temperatures below 450 °C. This is accompanied with a reduction of *J*$_{sc}$ from 16.9 mA/cm^2 over 15.6 mA/cm^2 to 10.8 mA/cm^2 for the forward sweep. The *V*$_{oc}$ saturated at 1 V except for PSCs using TiO$_2$ layer fabricated at temperatures above 150 °C. In contrast, the *V*$_{oc}$ of **A-150** PSCs decreased to 0.65 V, due to an inhomogeneous c-TiO$_2$ layer resulting in shunts. Simultaneously, the serial resistance increased from 6.7 Ω cm^2 to 7.5 Ω cm^2 and 9.6 Ω cm^2 with respect to decreasing deposition temperature. Representative *J-V* curves (forward and reverse sweep) for A-150, A-270 and A-360 PSCs can be found in Figure S3d) – f). The increasing series resistance and bulk resistivity resulting from thicker TiO$_2$ layers could be a plausible explanation for the decreasing *J*$_{sc}$ and PCE values at lower deposition temperatures.

14

Focusing on the PSC obtained from **A-150** sample, low transmittance of the TiO$_2$ layers explains the drop in PCE (Figure S1).

EQE measurements were performed on representative PSCs using **A-150**, **A-270** and **A-360** (Figure 5b). Figure 5b shows that the EQE of **A-270** and **A-360** PSCs are close to each other but the **A-150** PSC showed less than half of EQE in the range from 320 to 820 nm compared to **A-270** and **A-360**. For quantitative comparison the integrated J_{sc} was calculated using the following equation:

$$J_{sc} = q \ \int \Phi(\lambda) \times EQE(\lambda) \ d\lambda \qquad\qquad (1)$$

where q, Φ, λ, and EQE are charge of an electron, photon flux (in photons per area, time and wavelength interval), wavelength and the measured external quantum efficiency, respectively. Equation 1 was used for the determination of the integrated J_{sc} for **A-150**, **A-270** and **A-360** for both set-ups. They present the same trend as the PCE in the *J-V* measurements with similar integrated J_{sc} of ~14.9 mA/cm^2 for A-360 and A-270 and 6.3 mA/cm^2 for A-150.

To determine the solar cell performance under steady-state conditions, maximum power point tracking was done at 0.77 V for 180 s for a representative PSC of **A-360** and **A-270** (Figure S4). Figure S4a) and b) shows that both PSCs reach their maximum output after 50 to 60 s and kept virtually constant. The estimated power conversion of 12.1 % and 11.4 % for A-360 and A-270, respectively, are in the range of the photovoltaic parameters obtained from *J-V* curves.

CONCLUSION

In conclusion, we showed that tuning precursor chemistry in spray pyrolysis is a promising approach for optimizing the material properties of c-TiO$_2$ layers used as ETMs in hybrid PSC to improve photovoltaic performance. The impact of precursor chemistry was observed in

15

smoother TiO_2 layers with improved surface coverage and reduced pinholes when using $TiCl_4$ solution instead of the widely reported TDBA precursor. Solar cells fabricated using smoother layers ($TiCl_4$, 450 °C) exhibited increased fill factors (forward sweep), however the PSCs were still inferior in regard to PCEs compared to the devices prepared by TDBA (450 °C). Moreover, the gradual decrease of substrate temperature using $TiCl_4$ solution in the spray pyrolysis process indicates the potential of this process for energy efficient processing. A decrease in substrate temperature (360 °C) resulted in PCEs equal to the reference PCEs (TDBA, 450 °C). Further decrease of fabrication temperature to 150 °C for $TiCl_4$ based coatings, necessary for polymer substrates, resulted in a cracked thick layer, which exhibited low light transmittance and low device efficiencies, thus illustrating exemplary the trade-off between low-temperature synthesis of ETMs and decrease in PCE.

ACKNOWLEDGEMENT

SUPPLEMENTARY MATERIAL

See supplementary material for the complete fabrication and characterization process, transmission spectra, four point probe measurements, forward and reverse *J-V* scans, EQE spectra, integrated J_{sc} values and MPP tracking of solar cells.

REFERENCES

[1] W. S. Yang, J. H. Noh, N. J. Jeon, Y. C. Kim, S. Ryu, J. Seo and S. I. Seok, *Sci*, **2015**, *348*, 1234-1237.

[2] W. S. Yang, B.-W. Park, E. H. Jung, N. J. Jeon, Y. C. Kim, D. U. Lee, S. S. Shin, J. Seo, E. K. Kim, J. H. Noh and S. I. Seok, *Sci*, **2017**, *356*, 1376-1379.

[3] M. A. Green, A. Ho-Baillie and H. J. Snaith, *Nat Photon*, **2014**, *8*, 506-514.

[4] N.-G. Park, *J. Phys. Chem. Lett.*, **2013**, *4*, 2423-2429.

[5] J. M. Azpiroz, E. Mosconi, J. Bisquert and F. De Angelis, *Energy Environ Sci.*, **2015**, *8*, 2118-2127.

[6] E. Edri, S. Kirmayer, A. Henning, S. Mukhopadhyay, K. Gartsman, Y. Rosenwaks, G. Hodes and D. Cahen, *Nano Lett.*, **2014**, *14*, 1000-1004.

[7] Y. Liu, J. Sun, Z. Yang, D. Yang, X. Ren, H. Xu, Z. Yang and S. Liu, *Adv. Opt. Mater.*, **2016**, *4*, 1829-1837.

[8] T. M. Koh, K. Fu, Y. Fang, S. Chen, T. C. Sum, N. Mathews, S. G. Mhaisalkar, P. P. Boix and T. Baikie, *J. Phys. Chem. C*, **2014**, *118*, 16458-16462.

[9] J.-W. Lee, D.-H. Kim, H.-S. Kim, S.-W. Seo, S. M. Cho and N.-G. Park, *Adv. Eng. Mater.*, **2015**, *5*, 1501310-n/a.

[10] Y. Bekenstein, B. A. Koscher, S. W. Eaton, P. Yang and A. P. Alivisatos, *J. Am. Chem. Soc.*, **2015**, *137*, 16008-16011.

[11] H.-R. Xia, J. Li, W.-T. Sun and L.-M. Peng, *Chem. Commun.*, **2014**, *50*, 13695-13697.

[12] D. Gedamu, I. M. Asuo, D. Benetti, M. Basti, I. Ka, S. G. Cloutier, F. Rosei and R. Nechache, *Scientific Reports*, **2018**, *8*, 12885.

[13] B.-W. Park, B. Philippe, X. Zhang, H. Rensmo, G. Boschloo and E. M. J. Johansson, *Adv. Mater.*, **2015**, *27*, 6806-6813.

[14] S. Öz, J.-C. Hebig, E. Jung, T. Singh, A. Lepcha, S. Olthof, F. Jan, Y. Gao, R. German, P. H. M. van Loosdrecht, K. Meerholz, T. Kirchartz and S. Mathur, *Sol. Energy Mater. Sol. Cells*, **2016**, *158*, 195-201.

[15] M. H. Kumar, S. Dharani, W. L. Leong, P. P. Boix, R. R. Prabhakar, T. Baikie, C. Shi, H. Ding, R. Ramesh, M. Asta, M. Graetzel, S. G. Mhaisalkar and N. Mathews, *Adv. Mater.*, **2014**, *26*, 7122-7127.

[16] D. Sabba, H. K. Mulmudi, R. R. Prabhakar, T. Krishnamoorthy, T. Baikie, P. P. Boix, S. Mhaisalkar and N. Mathews, *J. Phys. Chem. C*, **2015**, *119*, 1763-1767.

[17] J.-H. Im, I.-H. Jang, N. Pellet, M. Grätzel and N.-G. Park, *Nat Nano*, **2014**, *9*, 927-932.

[18] H.-S. Kim and N.-G. Park, *J. Phys. Chem. Lett.*, **2014**, *5*, 2927-2934.

[19] S. Ryu, J. H. Noh, N. J. Jeon, Y. Chan Kim, W. S. Yang, J. Seo and S. I. Seok, *Energy Environ Sci.*, **2014**, *7*, 2614-2618.

[20] X. Song, W. Wang, P. Sun, W. Ma and Z.-K. Chen, *Appl. Phys. Lett.*, **2015**, *106*, 033901.

[21] M. Saliba, T. Matsui, J.-Y. Seo, K. Domanski, J.-P. Correa-Baena, M. K. Nazeeruddin, S. M. Zakeeruddin, W. Tress, A. Abate, A. Hagfeldt and M. Gratzel, *Energy Environ Sci.*, **2016**, *9*, 1989-1997.

[22] R. J. Sutton, G. E. Eperon, L. Miranda, E. S. Parrott, B. A. Kamino, J. B. Patel, M. T. Hörantner, M. B. Johnston, A. A. Haghighirad, D. T. Moore and H. J. Snaith, *Adv. Energy Mater.*, **2016**, *6*, 1502458-n/a.

[23] Q. Deng, Y. Li, L. Chen, S. Wang Gaosheng, G. Wang, S. Yonglong and G. Shao, *The effects of electron and hole transport layer with the electrode work function on perovskite solar cells*, **2016**.

[24] K. Mahmood, S. Sarwar and M. T. Mehran, *RSC Advances*, **2017**, *7*, 17044-17062.

[25] W. C. Lin, A. Kovalsky, Y. C. Wang, L. L. Wang, S. Goldberg, W. L. Kao, C. Y. Wu, H. Y. Chang, J. J. Shyue and C. Burda, *PCCP*, **2017**.

[26] S. Paek, P. Qin, Y. Lee, K. T. Cho, P. Gao, G. Grancini, E. Oveisi, P. Gratia, K. Rakstys, S. A. Al-Muhtaseb, C. Ludwig, J. Ko and M. K. Nazeeruddin, *Adv. Mater.*, 1606555-n/a.

[27] H.-S. Rao, B.-X. Chen, W.-G. Li, Y.-F. Xu, H.-Y. Chen, D.-B. Kuang and C.-Y. Su, *Adv. Funct. Mater.*, **2015**, *25*, 7200-7207.

[28] G. Murugadoss, H. Kanda, S. Tanaka, H. Nishino, S. Ito, H. Imahori and T. Umeyama, *J. Power Sources*, **2016**, *307*, 891-897.

[29] Y.-h. Zhao, K.-c. Zhang, Z.-w. Wang, P. Huang, K. Zhu, Z.-d. Li, D.-h. Li, L.-g. Yuan, Y. Zhou and B. Song, *ACS Appl. Mater. Interfaces*, **2017**.

[30] D.-Y. Son, J.-H. Im, H.-S. Kim and N.-G. Park, *J. Phys. Chem. C*, **2014**, *118*, 16567-16573.

[31] K. Mahmood, B. S. Swain, A. R. Kirmani and A. Amassian, *J. Mater. Chem. A*, **2015**, *3*, 9051-9057.

[32] F. Cai, L. Yang, Y. Yan, J. Zhang, F. Qin, D. Liu, Y.-B. Cheng, Y. Zhou and T. Wang, *J. Mater. Chem. A*, **2017**, *5*, 9402-9411.

[33] H. J. Snaith, A. Abate, J. M. Ball, G. E. Eperon, T. Leijtens, N. K. Noel, S. D. Stranks, J. T.-W. Wang, K. Wojciechowski and W. Zhang, *J. Phys. Chem. Lett.*, **2014**, *5*, 1511-1515.

[34] W. Ke, G. Fang, J. Wang, P. Qin, H. Tao, H. Lei, Q. Liu, X. Dai and X. Zhao, *ACS Appl. Mater. Interfaces*, **2014**, *6*, 15959-15965.

[35] W. Yongzhen, Y. Xudong, C. Han, Z. Kun, Q. Chuanjiang, L. Jian, P. Wenqin, I. Ashraful, B. Enbing, Y. Fei, Y. Maoshu, Z. Peng and H. Liyuan, *Appl. Phys. Express*, **2014**, *7*, 052301.

[36] S. Hong, A. Han, E. C. Lee, K.-W. Ko, J.-H. Park, H.-J. Song, M.-H. Han and C.-H. Han, *CAP*, **2015**, *15*, 574-579.

[37] T. Supasai, N. Henjongchom, I. M. Tang, F. Deng and N. Rujisamphan, *SoEn*, **2016**, *136*, 515-524.

[38] A. K. Jena, H.-W. Chen, A. Kogo, Y. Sanehira, M. Ikegami and T. Miyasaka, *ACS Appl. Mater. Interfaces*, **2015**, *7*, 9817-9823.

[39] H. Hu, B. Dong, H. Hu, F. Chen, M. Kong, Q. Zhang, T. Luo, L. Zhao, Z. Guo, J. Li, Z. Xu, S. Wang, D. Eder and L. Wan, *ACS Appl. Mater. Interfaces*, **2016**, *8*, 17999-18007.

[40] L. Escoubas, J. J. Simon, J. Le Rouzo and V. Bermudez, in *Optical Thin Films and Coatings*, eds. A. Piegari and F. Flory, Woodhead Publishing, 2013, pp. 596-630.

[41] J B Mooney and S. B. Radding, *Annu. Rev. Mater. Sci.*, **1982**, *12*, 81-101.

[42] P. S. Patil, *Mater. Chem. Phys.*, **1999**, *59*, 185-198.

[43] Z. Liu, Q. Chen, Z. Hong, H. Zhou, X. Xu, N. De Marco, P. Sun, Z. Zhao, Y.-B. Cheng and Y. Yang, *ACS Appl. Mater. Interfaces*, **2016**, *8*, 11076-11083.

[44] M. T. Masood, C. Weinberger, J. Sarfraz, E. Rosqvist, S. Sandén, O. J. Sandberg, P. Vivo, G. Hashmi, P. D. Lund, R. Österbacka and J.-H. Smått, *ACS Appl. Mater. Interfaces*, **2017**, *9*, 17906-17913.

[45] V. Ostapchenko, Q. Huang, O. Zhang and C. Zhao, *Int. J. Electroch. Sci.*, **2017**, *12*, 2262-2271.

[46] A. Yella, L.-P. Heiniger, P. Gao, M. K. Nazeeruddin and M. Grätzel, *Nano Lett.*, **2014**, *14*, 2591-2596.

[47] X. Dai, C. Shi, Y. Zhang and N. Wu, *J. Semicond.*, **2015**, *36*, 074003.

[48] P. Vivo, A. Ojanperä, J.-H. Smått, S. Sandén, S. G. Hashmi, K. Kaunisto, P. Ihalainen, M. T. Masood, R. Österbacka, P. D. Lund and H. Lemmetyinen, *Org. Electron.*, **2017**, *41*, 287-293.

[49] H. Tan, A. Jain, O. Voznyy, X. Lan, F. P. García de Arquer, J. Z. Fan, R. Quintero-Bermudez, M. Yuan, B. Zhang, Y. Zhao, F. Fan, P. Li, L. N. Quan, Y. Zhao, Z.-H. Lu, Z. Yang, S. Hoogland and E. H. Sargent, *Sci*, **2017**, *355*, 722-726.

[50] H. Zhou, Q. Chen, G. Li, S. Luo, T.-b. Song, H.-S. Duan, Z. Hong, J. You, Y. Liu and Y. Yang, *Sci*, **2014**, *345*, 542-546.

[51] S. D. Stranks, G. E. Eperon, G. Grancini, C. Menelaou, M. J. P. Alcocer, T. Leijtens, L. M. Herz, A. Petrozza and H. J. Snaith, *Sci*, **2013**, *342*, 341-344.

[52] D. Bi, W. Tress, M. I. Dar, P. Gao, J. Luo, C. Renevier, K. Schenk, A. Abate, F. Giordano, J.-P. Correa Baena, J.-D. Decoppet, S. M. Zakeeruddin, M. K. Nazeeruddin, M. Grätzel and A. Hagfeldt, *Sci. Adv.*, **2016**, *2*.

[53] D. A. C. A. R.R.L. De Oliveira, T.G.S. Cruz, F.M. Yamaji, F.L. Leite ed. D. V. Bellitto, **2012**, ch. 7.

[54] J. A. Christians, J. S. Manser and P. V. Kamat, *J. Phys. Chem. Lett.*, **2015**, *6*, 852-857.